Cytoplasmic Dynein Moves Through Uncoordinated Stepping of the AAA+ Ring Domains

Mark A. DeWitt *et al.*

Science **335**, 221 (2012);
DOI: 10.1126/science.1215804

Science (print ISSN 0036-8075; online ISSN 1095-9203) is published weekly, except the last week in December, by the American Association for the Advancement of Science, 1200 New York Avenue NW, Washington, DC 20005.

ancestry of micronemes (*24*, *25*). Although PfDOC2.1 knockdown in *P. falciparum* has a clear effect on invasion, at this level of knockdown it did not result in an egress defect, suggesting that *Plasmodium* merozoites may rely on microneme secretion for invasion but on qualitatively different exoneme secretion for egress from the erythrocyte (*26*). However, in *Toxoplasma* mutant F-P2 both invasion and egress were defective because microneme secretion plays a central role in both of these processes (*27*), highlighting divergent roles for secretory organelles in egress between these organisms. This multilayered Ca^{2+}-mediated control of microneme secretion may underscore tight temporal regulation, and this mechanism appears ancestral to the ciliates and the Apicomplexa.

References and Notes

1. J. Baum, T. W. Gilberger, F. Frischknecht, M. Meissner, *Trends Parasitol.* **24**, 557 (2008).
2. K. Nagamune, S. N. Moreno, E. N. Chini, L. D. Sibley, *Subcell. Biochem.* **47**, 70 (2008).
3. J. D. Dvorin *et al.*, *Science* **328**, 910 (2010).
4. S. Lourido *et al.*, *Nature* **465**, 359 (2010).
5. M. J. Gubbels *et al.*, *PLoS Pathog.* **4**, e36 (2008).
6. K. P. Eidell, T. Burke, M. J. Gubbels, *Mol. Biochem. Parasitol.* **171**, 97 (2010).
7. M. G. Del Carmen, M. Mondragón, S. González, R. Mondragón, *Cell. Microbiol.* **11**, 967 (2009).
8. V. B. Carruthers, S. N. Moreno, L. D. Sibley, *Biochem. J.* **342**, 379 (1999).
9. Materials and methods are available as supporting material on *Science* Online.
10. S. Håkansson, H. Morisaki, J. Heuser, L. D. Sibley, *Mol. Biol. Cell* **10**, 3539 (1999).
11. K. L. Carey, N. J. Westwood, T. J. Mitchison, G. E. Ward, *Proc. Natl. Acad. Sci. U.S.A.* **101**, 7433 (2004).
12. M. H. Huynh, V. B. Carruthers, *PLoS Pathog.* **2**, e84 (2006).
13. S. Hegge *et al.*, *FASEB J.* **24**, 2222 (2010).
14. S. Münter *et al.*, *Cell Host Microbe* **6**, 551 (2009).
15. J. L. Lovett, N. Marchesini, S. N. Moreno, L. D. Sibley, *J. Biol. Chem.* **277**, 25870 (2002).
16. D. M. Wetzel, L. A. Chen, F. A. Ruiz, S. N. Moreno, L. D. Sibley, *J. Cell Sci.* **117**, 5739 (2004).
17. D. R. Smith *et al.*, *Genome Res.* **18**, 1638 (2008).
18. S. Martens, *Biochem. Soc. Trans.* **38**, 213 (2010).
19. W. Cho, R. V. Stahelin, *Biochim. Biophys. Acta* **1761**, 838 (2006).
20. R. Friedrich, A. Yeheskel, U. Ashery, *Mol. Neurobiol.* **41**, 42 (2010).
21. A. J. Groffen *et al.*, *Science* **327**, 1614 (2010).
22. S. Martens, H. T. McMahon, *Natl. Rev.* **9**, 543 (2008).
23. L. A. Banaszynski, L. C. Chen, L. A. Maynard-Smith, A. G. Ooi, T. J. Wandless, *Cell* **126**, 995 (2006).
24. C. Erxleben, H. Plattner, *J. Cell Biol.* **127**, 935 (1994).
25. B. S. Leander, P. J. Keeling, *Trends Ecol. Evol.* **18**, 395 (2003).
26. K. Koussis *et al.*, *EMBO J.* **28**, 725 (2009).
27. B. F. Kafsack *et al.*, *Science* **323**, 530 (2009).
28. G. T. Marth *et al.*, *Nat. Genet.* **23**, 452 (1999).

Acknowledgments: We thank C. Nussbaum and C. Russ of the "Broad Sequencing Platform" and D. Sibley, J.-F. Dubremetz, M.-F. Cesbron-Delauw, J.-C. Doury, and M. Makler (Flow Inc.) for kindly sharing reagents. F-P2 was originally generated in the laboratory of B. Striepen. This work was supported by National Institutes of Health grants AI081220 to M.-J.G. and G.T.M., AI057919 and AI088314 to M.T.D., HG004719 to G.T.M., and AI087874 to J.D.D.; a Knights Templar Eye Foundation grant to S.T., a Wellcome Trust equipment grant to D.J.P.F., a Burroughs Wellcome Fund New Investigator in the Pathogenesis of Infectious Disease Fellowship to M.T.D., and an American Heart Association Scientist Development Grant (0635480N) to M.-J.G. *Toxoplasma gondii* GT1 sequence and annotation are from L. Caler at the J. Craig Venter Institute. Sequence reads have been deposited at the National Center for Biotechnology Information sequence read archive under accession no. SRA046023.

Supporting Online Material

www.sciencemag.org/cgi/content/full/335/6065/218/DC1
Materials and Methods
Figs. S1 to S12
Tables S1 to S2
References (*29*–*54*)
Movies S1 to S4

7 July 2011; accepted 29 November 2011
10.1126/science.1210829

Cytoplasmic Dynein Moves Through Uncoordinated Stepping of the AAA+ Ring Domains

Mark A. DeWitt, Amy Y. Chang, Peter A. Combs, Ahmet Yildiz*

Cytoplasmic dynein is a homodimeric AAA+ motor that transports a multitude of cargos toward the microtubule minus end. How the two catalytic head domains interact and move relative to each other during processive movement is unclear. Here, we tracked the relative positions of both heads with nanometer precision and directly observed the heads moving independently along the microtubule. The heads remained widely separated, and their stepping behavior varied as a function of interhead separation. One active head was sufficient for processive movement, and an active head could drag an inactive partner head forward. Thus, dynein moves processively without interhead coordination, a mechanism fundamentally distinct from the hand-over-hand stepping of kinesin and myosin.

Cytoplasmic dynein forms a 1.2-MD complex that uses adenosine triphosphate (ATP) hydrolysis to power minus-end–directed motility along microtubules. The catalytic head domain is composed of six AAA+ [adenosine triphosphatases (ATPases) associated with diverse cellular activities] modules arranged in a ring (*1*). ATPase activity at AAA1 is essential for dynein motility (*2*). The two rings are connected by the dimerization of N-terminal tail domains and bind to the microtubule through a ~15-nm coiled-coil stalk bearing a small microtubule-binding domain (MTBD). Dynein is required for many cellular processes, including organelle transport and cell division, and dynein malfunction can lead to motor neuron degeneration (*3*).

Despite recent advances in understanding dynein's structure (*4*) and mechanism (*5*, *6*), the stepping mechanism of dimeric dynein during processive motion remains unclear. Studies of kinesin and myosin motors have shown that their heads take alternating steps in a hand-over-hand (HoH) fashion (*7*–*9*). Dynein motility also requires two heads (*6*), but it is unclear whether they coordinate with each other to achieve processive motion (*10*). Dynein's structure and origin are distinct from kinesin and myosin, suggesting that it may use a different mechanism.

To investigate dynein's stepping mechanism, we tracked the movement of an artificially dimerized, tail-truncated yeast cytoplasmic dynein [glutathione *S*-transferase–Dyn_{331kD} (GST-Dyn_{331kD})], which has similar stepping properties to native dynein (*6*). First, we tracked the movement of dynein labeled with a single quantum dot (QD) at 2 msec temporal resolution in the presence of rate-limiting ATP (Fig. 1A and fig. S1). As reported previously (*5*, *6*), the distribution of step sizes was multimodal. The step-size histogram of head-labeled dynein revealed two major peaks at 9.3 ± 0.7 and 17.5 ± 1.2 nm that were nearly twice as large as the peaks observed in the tail histogram (4.8 ± 0.3 and 8.7 ± 0.9 nm) (Fig. 1B). The probability of backward stepping (p_{BW}) was 0.2. The dwell-time histogram for head-labeled dynein at 12 μM ATP (Fig. 1C) was best fit by a convolution of one slow ($k_1 = 2.1 \pm 0.2$ sec^{-1}) and one fast ($k_2 = 14.1 \pm 2.5$ sec^{-1}) exponential rate constant. The product of k_2 and the average head step size ($d_{head} = 10.2$ nm) agrees well with the average velocity of dynein at saturating [ATP] (124 nm/sec). This data excludes the symmetric HoH model, which predicts the stepping kinetics of a head to be a convolution of two equal rate constants (fig. S2). Instead, the dwell-time histogram of tail-labeled dynein was well described by a kinetic model in which the heads can step independently and the tail moves each time either head takes a step ($k'_1 = 1.2 \pm 0.1$ sec^{-1}; $k'_2 = 12.2 \pm 2.7$ sec^{-1}) (fig. S2).

To directly address how the two heads interact and move relative to each other, we labeled GST-Dyn_{331kD} with different-colored QDs (17 to 22 nm in size) (table S1) at the C termini and simultaneously tracked the positions of the heads during processive movement (*11*). The fluorescent signal was split into two channels and registered

Department of Physics, and Department of Molecular and Cellular Biology, University of California, Berkeley, CA 94720, USA.

*To whom correspondence should be addressed. E-mail: yildiz@berkeley.edu

to 3-nm precision (figs. S3 to S5). Representative traces (Fig. 2A, fig. S6, and movies S1 and S2) clearly showed that either head could take a step regardless of which head was leading, a mechanism distinct from HoH. Although most steps showed a canonical alternating pattern, one head could take multiple consecutive (nonalternating) steps before the other head moved (Fig. 2B). Nonalternating stepping occurred about half as often as alternating stepping (32% of steps, fig. S7). This may partly be due to the time needed for a head to complete its ATPase cycle before it can take another step.

The heads often walked along different protofilaments (fig. S6), with the leading head preferentially located to the right of the trailing head (Fig. 2C and fig. S8). Measurements using organic dyes showed that the heads were separated by 23.0 ± 13.2 nm (mean ± SD) (fig. S9), excluding the possibility of a stacking interaction between the AAA+ rings (*12*).

The heads frequently swapped the lead, but not strictly after every step of the motor. The stepping characteristics of a head in the leading and trailing positions differed substantially depending on interhead separation, forming the basis of the high variability in dynein's step size (*6*). The on-axis (parallel to the microtubule long axis) step size decreased by ~0.4 nm per nanometer increase in interhead separation (Fig. 3A). The trailing head took larger (d = 17.5 nm) forward and fewer (p_{BW} = 0.14) backward steps. In contrast, the leading head took significantly shorter (d = 1.5 nm) forward and more frequent (p_{BW} = 0.45) backward steps. The off-axis (perpendicular to the microtubule long axis) step size also decreased with interhead separation but without a net bias toward left or right (Fig. 3B). The stepping probabilities of the leading and trailing heads were nearly identical when they were positioned close (10 to 20 nm) to each other. At larger separations, 65% of the steps were taken by the trailing head (Fig. 3C).

The heads of native dynein also moved independently, and their stepping behavior varied as a function of interhead separation, similar to GST-Dyn$_{331kD}$ (figs. S10 and S11). The results show that the tail domain is not involved in interhead coordination.

Our results show that dynein's stepping mechanism is different from processive kinesins and myosins. The stepping motion of these motors is driven by the power stroke of the bound head, which moves the trailing head forward. For dynein, we propose a tethered excursion model (Fig. 3D), in which a conformational change that produces the minus-end bias occurs in the unbound head. Either head can bind ATP at the AAA1 site, followed by its release from the microtubule (*13*). The linker undergoes a minus-end–directed priming stroke upon ATP hydrolysis (*14*), which moves its MTBD forward. The large and flexible linker allows the released head to diffuse over a wide area, resulting in both large interhead separations and variable step sizes.

The heads experience intramolecular tension at large separations, and the power stroke of the bound head may occasionally trigger the release of the other head. In fact, we observed that the stepping probability of the trailing head increased at large separations (Fig. 3C). This result is consistent with force-induced movement of dynein, which requires less force when it is pulled toward the minus end (*15*). In addition, tension can bias the diffusional search of the tethered head toward the bound head, preventing further extension of the dimer (Fig. 3D).

The tethered excursion model predicts that a single force-generating head in a dynein dimer can both take a step and drag an inactive head forward. We tested the motility of a heterodimeric dynein with one wild-type head (WT$_h$) and one mutant head lacking the ability to hydrolyze ATP at the AAA1 domain (Mut$_h$) (*6*, *16*). Mut$_h$

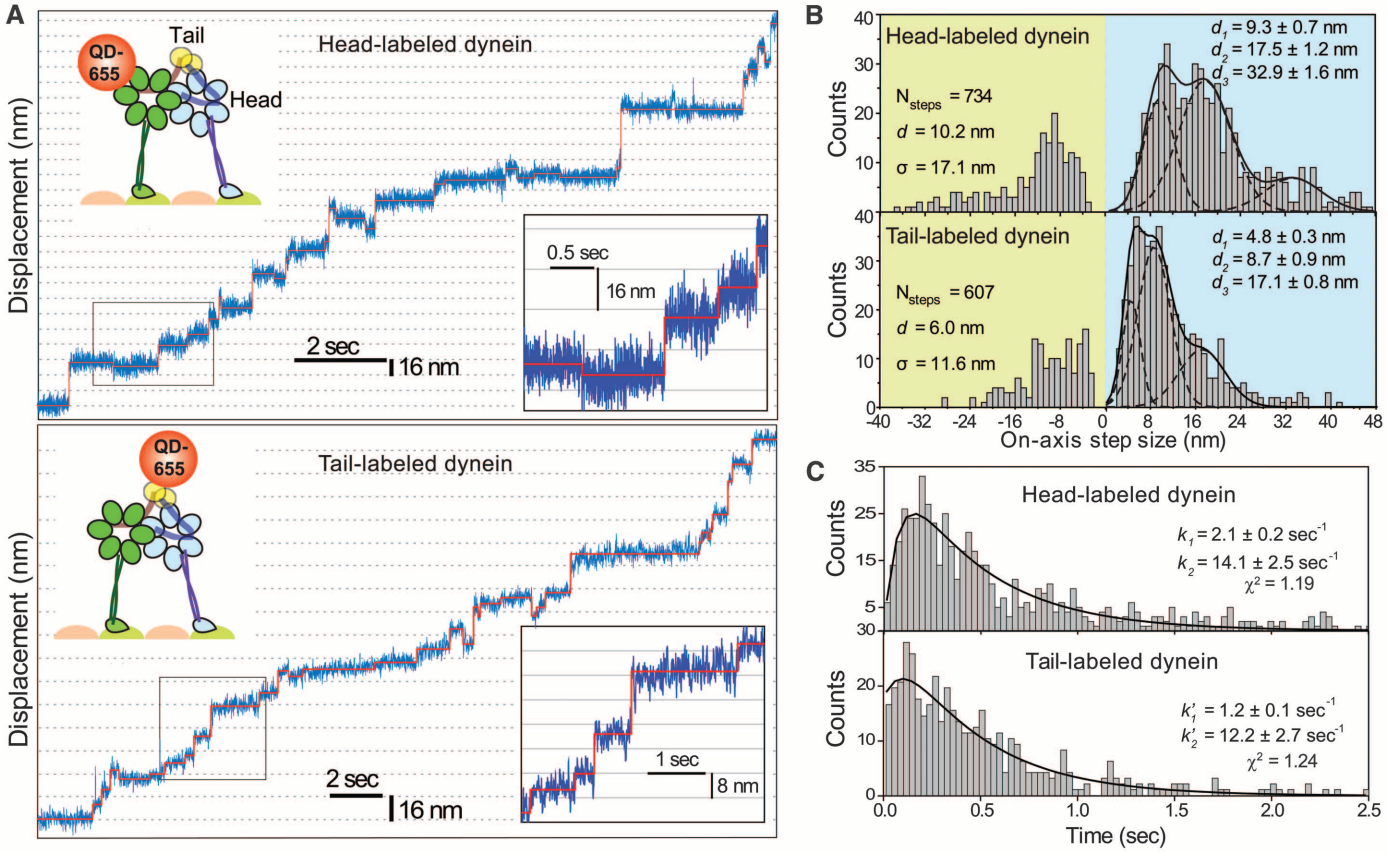

Fig. 1. (**A**) Step-size measurements of tail- and head-labeled GST-Dyn$_{331kD}$ with a single QD-655 at 2-msec temporal resolution. The QD position (blue traces) was fit by a step-finding algorithm (solid red lines). (**B**) Multiple Gaussian fits to step-size histograms reveal two major peaks at 9.3 and 17.5 nm for the head and 4.8 and 8.7 nm for the tail. (**C**) Dwell-time histogram of head-stepping fitted to a convolution of two unequal rate constants and that of tail-stepping fitted to a model assuming uncoordinated stepping between two heads, each with two unequal rate constants.

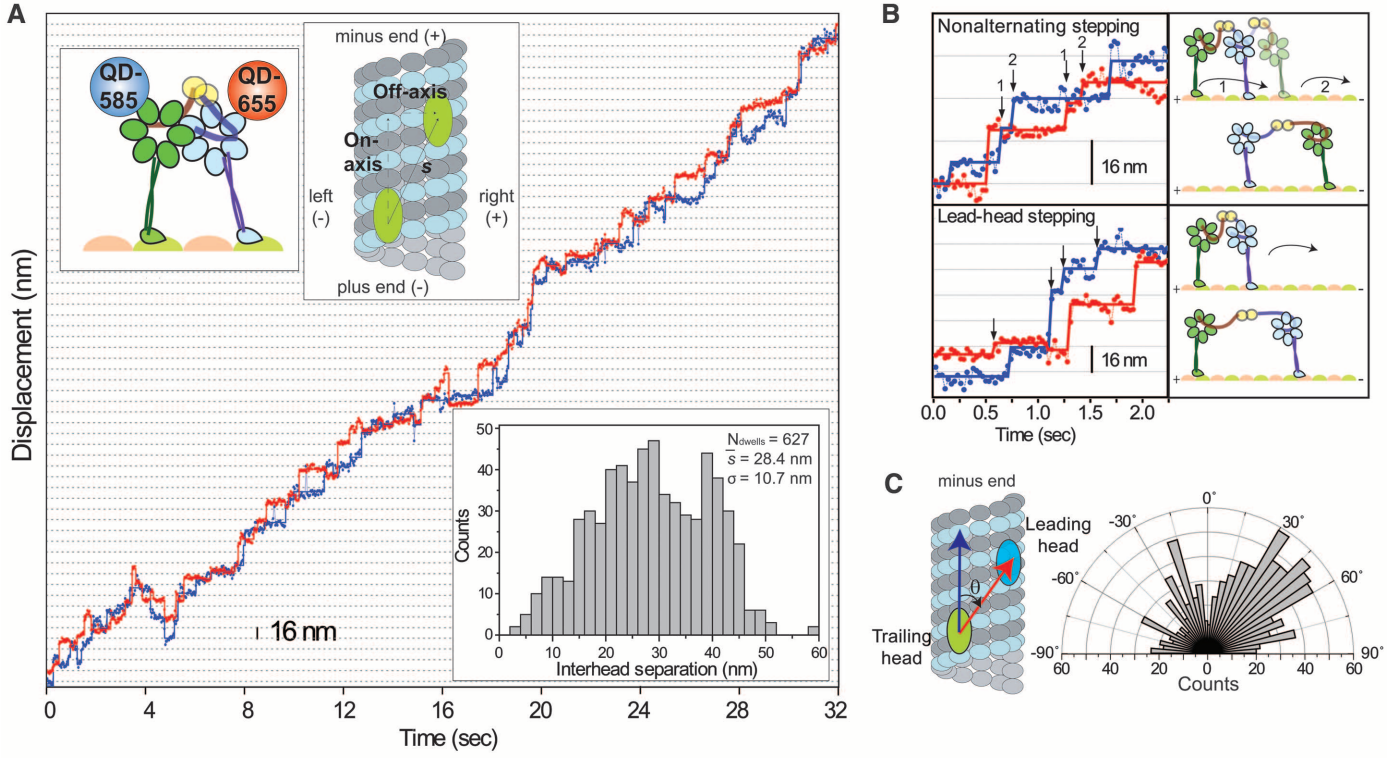

Fig. 2. (**A**) Stepping trace of GST-Dyn$_{331kD}$ labeled with QD-585 (blue) and QD-655 (red) shows that the heads move independently of each other during processive runs. The heads are separated by 28.4 ± 10.7 nm (bottom inset). (**B**) Examples of nonalternating and lead-head stepping (arrows) show that dynein stepping deviates from the HoH mechanism. (**C**) Histogram of the angles between the interhead separation vector (red arrow) and the microtubule long axis (blue arrow).

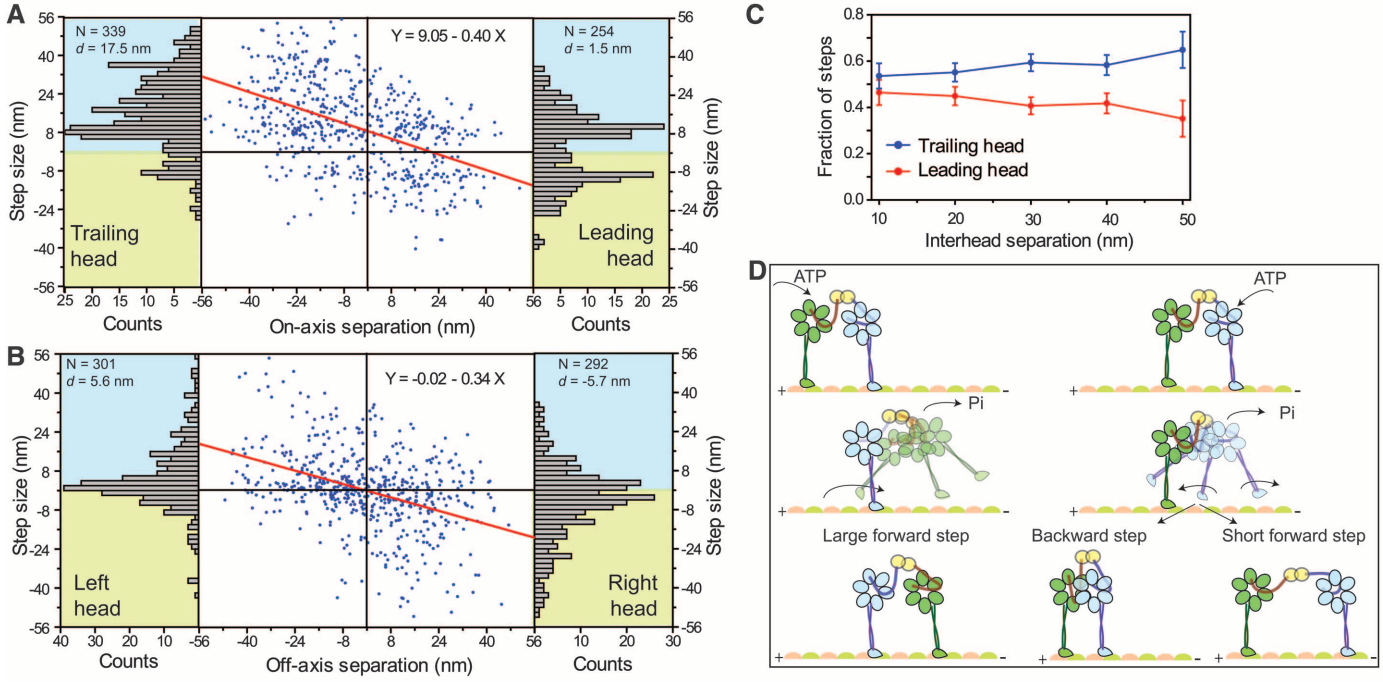

Fig. 3. (**A**) The on-axis step size (blue dots) of GST-Dyn$_{331kD}$ decreases linearly (red line) as a function of interhead separation and is biased forward by 9.1 ± 0.6 nm. The leading head takes shorter (d = 1.5 nm) steps with more frequent (p_{BW} = 0.45) backward steps, compared with the trailing head (d = 17.5 nm; p_{BW} = 0.14) (bar graphs). (**B**) Off-axis step sizes show a linear dependence on interhead separation without a bias to move toward the right (positive) or left (negative). (**C**) Fraction of the steps taken by the leading and trailing heads at different interhead separations (mean ± SEM). (**D**) Tethered excursion model for the dynein stepping mechanism. Either the leading or the trailing head can hydrolyze ATP and release from the microtubule. A diffusional search of the trailing head (green) is biased forward by interhead tension and the linker swing, resulting in a large forward step. In contrast, linker swing and tension bias the diffusion of the leading head (blue) in opposing directions, resulting in either a backward step or a short forward step.

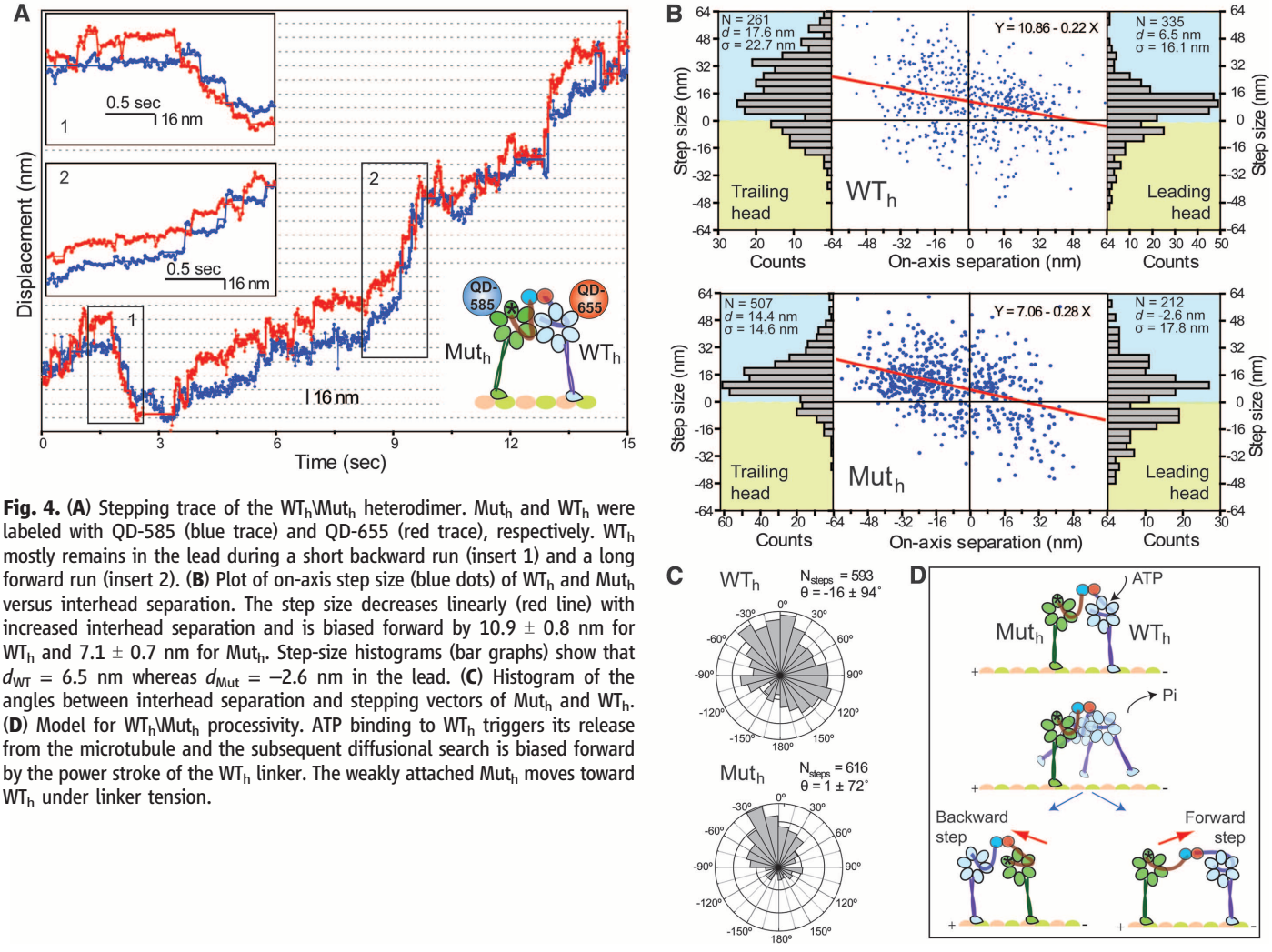

Fig. 4. (**A**) Stepping trace of the WT$_h$\Mut$_h$ heterodimer. Mut$_h$ and WT$_h$ were labeled with QD-585 (blue trace) and QD-655 (red trace), respectively. WT$_h$ mostly remains in the lead during a short backward run (insert 1) and a long forward run (insert 2). (**B**) Plot of on-axis step size (blue dots) of WT$_h$ and Mut$_h$ versus interhead separation. The step size decreases linearly (red line) with increased interhead separation and is biased forward by 10.9 ± 0.8 nm for WT$_h$ and 7.1 ± 0.7 nm for Mut$_h$. Step-size histograms (bar graphs) show that d_{WT} = 6.5 nm whereas d_{Mut} = –2.6 nm in the lead. (**C**) Histogram of the angles between interhead separation and stepping vectors of Mut$_h$ and WT$_h$. (**D**) Model for WT$_h$\Mut$_h$ processivity. ATP binding to WT$_h$ triggers its release from the microtubule and the subsequent diffusional search is biased forward by the power stroke of the WT$_h$ linker. The weakly attached Mut$_h$ moves toward WT$_h$ under linker tension.

cannot undergo a power stroke (*17*) and is weakly associated with the microtubule (*13*). The WT$_h$\Mut$_h$ heterodimer moved processively toward the microtubule minus end (movies S3 and S4, Fig. 4A, and figs. S12 and S13). WT$_h$ was found in the lead 66% of the time (fig. S14). Similarly, during occasional short (4 to 5 steps) backward runs, WT$_h$ remained in the leading position toward the plus end.

Mut$_h$ exhibited different stepping characteristics in both the leading and trailing positions (Fig. 4B) than WT$_h$. The on-axis step size of Mut$_h$ had reduced (7.1 ± 0.7 nm) minus-end–directed bias, compared with WT$_h$ (10.9 ± 0.8 nm). The probability of Mut$_h$ being in the lead decreased as interhead separation increased (<25% at 30+ nm separations) (fig. S15), and Mut$_h$ was more likely to step backward from the lead (d = –2.6 nm; p_{BW} = 0.44) (Fig. 4B). The average step size and stepping rate of Mut$_h$ were similar to those of WT$_h$ (figs. S14 and S15). Mut$_h$ stepping was mostly directed toward WT$_h$, whereas the direction of WT$_h$ stepping was largely independent of the position of Mut$_h$ (Fig. 4C).

Thus, dynein motility does not require allosteric communication between the AAA1 sites, and only one force-generating head is sufficient for processive movement. WT$_h$ usually remains in the lead and drives forward movement. The detachment of Mut$_h$ from the microtubule can be facilitated by ATP binding to its AAA1 site (*13*). Alternatively, Mut$_h$ can release under tension generated through the power stroke of WT$_h$. Because Mut$_h$ lacks the ability to generate a power stroke, its step size is mainly biased toward the WT$_h$ under tension (Fig. 4D).

Our results challenge established views of motor processivity that require coordination between the mechanochemical cycles of the heads. Kinesin (*18*, *19*) and myosin (*20*) motility rely on mechanical and chemical gating mechanisms that allow the leading head to stay bound to its track while the trailing head moves forward. Dynein clearly moves by a different mechanism. We see no evidence of strict gating that keeps the heads out of phase. Processivity requires two heads to be physically connected (*6*) to prevent detachment of the motor when one of the heads steps forward. It is possible that simultaneous detachment of both heads is stochastic. Dynein's high duty ratio (*21*) may allow the motor to take many steps before dissociation. Processivity in the absence of gating is also achieved by multiple monomeric kinesins (*22*) and engineered dimeric motors that have poor mechanochemical communication between the heads (*18*, *23*). Further understanding of the molecular basis of dynein processivity will require simultaneous monitoring of the linker conformations and stepping motion of the leading and trailing head domains.

References and Notes

1. S. A. Burgess, M. L. Walker, H. Sakakibara, P. J. Knight, K. Oiwa, *Nature* **421**, 715 (2003).
2. T. Kon, M. Nishiura, R. Ohkura, Y. Y. Toyoshima, K. Sutoh, *Biochemistry* **43**, 11266 (2004).
3. K. M. Ori-McKenney, J. Xu, S. P. Gross, R. B. Vallee, *Nat. Cell Biol.* **12**, 1228 (2010).
4. A. P. Carter, C. Cho, L. Jin, R. D. Vale, *Science* **331**, 1159 (2011).
5. R. Mallik, B. C. Carter, S. A. Lex, S. J. King, S. P. Gross, *Nature* **427**, 649 (2004).
6. S. L. Reck-Peterson *et al.*, *Cell* **126**, 335 (2006).
7. A. Yildiz *et al.*, *Science* **300**, 2061 (2003).
8. C. L. Asbury, A. N. Fehr, S. M. Block, *Science* **302**, 2130 (2003).
9. A. Yildiz, M. Tomishige, R. D. Vale, P. R. Selvin, *Science* **303**, 676 (2004).
10. D. Tsygankov, A. W. Serohijos, N. V. Dokholyan, T. C. Elston, *J. Chem. Phys.* **130**, 025101 (2009).

11. L. S. Churchman, Z. Okten, R. S. Rock, J. F. Dawson, J. A. Spudich, *Proc. Natl. Acad. Sci. U.S.A.* **102**, 1419 (2005).
12. D. Nicastro *et al.*, *Science* **313**, 944 (2006).
13. K. Imamula, T. Kon, R. Ohkura, K. Sutoh, *Proc. Natl. Acad. Sci. U.S.A.* **104**, 16134 (2007).
14. A. J. Roberts *et al.*, *Cell* **136**, 485 (2009).
15. A. Gennerich, A. P. Carter, S. L. Reck-Peterson, R. D. Vale, *Cell* **131**, 952 (2007).
16. C. Cho, S. L. Reck-Peterson, R. D. Vale, *J. Biol. Chem.* **283**, 25839 (2008).
17. T. Kon, T. Mogami, R. Ohkura, M. Nishiura, K. Sutoh, *Nat. Struct. Mol. Biol.* **12**, 513 (2005).
18. A. Yildiz, M. Tomishige, A. Gennerich, R. D. Vale, *Cell* **134**, 1030 (2008).
19. B. E. Clancy, W. M. Behnke-Parks, J. O. Andreasson, S. S. Rosenfeld, S. M. Block, *Nat. Struct. Mol. Biol.* **18**, 1020 (2011).
20. S. Nishikawa *et al.*, *Cell* **142**, 879 (2010).
21. T. Shima, K. Imamula, T. Kon, R. Ohkura, K. Sutoh, *J. Struct. Biol.* **156**, 182 (2006).
22. T. Kamei, S. Kakuta, H. Higuchi, *Biophys. J.* **88**, 2068 (2005).
23. J. C. Liao, M. W. Elting, S. L. Delp, J. A. Spudich, Z. Bryant, *J. Mol. Biol.* **392**, 862 (2009).

Acknowledgments: We thank R. D. Vale and A. P. Carter for providing yeast strains; T. Bilyard, F. B. Cleary, and S. Shih for critical evaluation of the manuscript; and K. Schimert for technical assisstance. This work is supported by NIH [GM094522 (A.Y.), GM08295 (M.A.D. and P.A.C.)], NSF [MCB-1055017 (A.Y.)], and Burroughs Wellcome Foundation (A.Y.).

Supporting Online Material

www.sciencemag.org/cgi/content/full/science.1215804/DC1
Materials and Methods
Figs. S1 to S15
Table S1
References (*24*–*29*)
Movies S1 to S4

26 October 2011; accepted 24 November 2011
Published online 8 December 2011;
10.1126/science.1215804

Tumor Necrosis Factor Signaling Requires iRhom2 to Promote Trafficking and Activation of TACE

Colin Adrain,[1]† Markus Zettl,[1]*† Yonka Christova,[1] Neil Taylor,[2] Matthew Freeman[1]‡

The cytokine tumor necrosis factor (TNF) is the primary trigger of inflammation. Like many extracellular signaling proteins, TNF is synthesized as a transmembrane protein; the active signal is its ectodomain, which is shed from cells after cleavage by an ADAM family metalloprotease, ADAM17 (TNFα-converting enzyme, TACE). We report that iRhom2 (RHBDF2), a proteolytically inactive member of the rhomboid family, is required for TNF release in mice. iRhom2 binds TACE and promotes its exit from the endoplasmic reticulum. The failure of TACE to exit the endoplasmic reticulum in the absence of iRhom2 prevents the furin-mediated maturation and trafficking of TACE to the cell surface, the site of TNF cleavage. Given the role of TNF in autoimmune and inflammatory diseases, iRhom2 may represent an attractive therapeutic target.

Proteolytic release of the extracellular domain of transmembrane proteins is an important mechanism for generating signals that regulate major aspects of animal development, physiology, immunity, and pathology (*1*, *2*). An important example of regulated ectodomain shedding is the cytokine tumor necrosis factor (TNF), the primary trigger of inflammatory responses. TNF is associated with many human diseases, including rheumatoid arthritis, Crohn's disease, atherosclerosis, psoriasis, sepsis, diabetes, and obesity. Its blockade is licensed as a therapy for a number of conditions and is being assessed for others (*3*). Soluble, active TNF is shed from the plasma membrane by the ADAM family metalloprotease TACE (TNFα-converting enzyme, also known as ADAM17) (*4*). Despite the medical importance of TNF and other transmembrane signaling proteins, the regulation of ectodomain shedding remains poorly understood. Both the transmembrane forms of the signaling proteins themselves and the shedding proteases are subject to control by posttranslational modification, interaction with specific partners, and regulated intracellular trafficking and compartmentalization (*5*–*9*). The relative physiological importance, however, of these different modes of regulation is unclear.

We have investigated the regulation of ectodomain shedding by genetic and cellular approaches, both in *Drosophila* and mammalian cells. This has led to the recent discovery of a new class of polytopic endoplasmic reticulum (ER) proteins, the iRhoms, which are noncatalytic relatives of rhomboid intramembrane proteases (Fig. 1A) (*10*). *Drosophila* iRhom regulates epidermal growth factor (EGF) receptor signaling by interacting with EGF family ligands in the ER, shunting them into the ER-associated degradation (ERAD) pathway (*11*). iRhoms are conserved in all metazoans, and in cell culture assays, their mammalian counterparts, iRhom1 and iRhom2, can also promote ERAD of EGF. In mammals, however, their physiological role is unknown. We therefore generated a null mutation in the gene that encodes iRhom2 (RHBDF2) in mice (*12*) (fig. S1A). *iRhom2*$^{-/-}$ (knockout, KO) mice appeared normal: They were viable and fertile, with no morphological defects. Unlike iRhom1, which is widely expressed, iRhom2 is predominantly expressed in immune cells, particularly macrophages (*13*, *14*), where its expression was specifically up-regulated in response to lipopolysaccharide (LPS) stimulation (Fig. 1B). We therefore challenged *iRhom2*$^{-/-}$ mice with LPS, to mimic bacterial infection, and measured the serum concentration of proinflammatory cytokines. Interleukin-1β (IL-1β), IL-6, and IL-12 were induced normally but, remarkably, TNF induction was almost completely abolished in mutant mice (Fig. 1C). Macrophages are the most abundant source of TNF; consistent with this, in vitro differentiated bone marrow–derived macrophages (BMDMs) from *iRhom2*$^{-/-}$ mice failed to secrete TNF in response to LPS (Fig. 1D).

The failure of TNF secretion in *iRhom2*$^{-/-}$ mice [confirmed in this issue; see (*15*)] is not caused by its loss of expression: RNA levels were unaffected (fig. S2A), and protein levels were actually elevated in *iRhom2*$^{-/-}$ macrophages (Fig. 2, A and B). This result was confirmed by cell surface labeling followed by affinity precipitation, which showed an increase in the accumulation of the full-length, membrane-tethered form of TNF on the plasma membrane of mutant cells (Fig. 2C). Furthermore, inhibition of the shedding protease TACE in wild-type (WT) cells by the matrix metalloproteinase inhibitor BB94 (Fig. 2, A and C) resulted in a phenotype similar to *iRhom2*$^{-/-}$ macrophages. Together, these data imply that loss of iRhom2 does not interfere with the induction or intracellular trafficking of TNF but instead suggests a shedding defect. We tested this hypothesis directly. Although TACE levels were normal in both WT and mutant macrophages (Fig. 2D), loss of iRhom2 led to a complete abolition of activity of immunoprecipitated TACE (Fig. 2E and fig. S2B). This result explains the loss of TNF shedding in mutant mice and macrophages.

Like TNF, TACE has been the focus of major pharmaceutical interest: Not only does it regulate inflammation through TNF, but it is also implicated in cancer by activating EGF receptor ligands (*16*); furthermore, it is a point of integration for a wide range of incoming signals (*17*). Despite this intense spotlight, TACE regulation remains poorly understood. Several lines of evidence suggest the trafficking of enzyme to the plasma membrane is important, but other work implies that, at least in some contexts, the rate-limiting step may be activation of molecules already at the cell surface (*5*–*7*, *18*, *19*). Because most evidence agrees that the plasma membrane is the primary site of TACE activity, we tested

[1]Medical Research Council Laboratory of Molecular Biology, Hills Road, Cambridge CB2 0QH, UK. [2]Cambridge Research Institute, Cancer Research UK, Li Ka Shing Centre, Robinson Way, Cambridge CB2 0RE, UK.

*Present address: Boehringer Ingelheim, NBE Discovery, Dr. Boehringer-Gasse 5-11, A-1121 Wien, Austria.
†These authors contributed equally to this work.
‡To whom correspondence should be addressed. E-mail: MF1@mrc-lmb.cam.ac.uk